UniScatter: Unifying Backscatter Communications, Symbiotic Radio and Reconfigurable Intelligent Surface

Yang Zhao, *Member, IEEE,* and Bruno Clerckx, *Fellow, IEEE*

Abstract—Scatterers can harvest energy from, modulate information over, and influence propagation of surrounding radio waves. Backscatter Communications (BackCom) varies object impedance to manipulate the magnitude, phase, and/or frequency of scattered signal to encode information and deliver within coverage. Reconfigurable Intelligent Surface (RIS) adapts scattering antennas or programmable metamaterial to control wireless propagation environment by boosting/suppressing signal strength in specific directions. Symbiotic Radio (SR) incorporates scatter nodes into active networks that recycle ambient signal to transmit self information and enhance legacy channel to the cooperative receiver. In this paper, we depart from those concepts and introduce UniScatter as a new paradigm for future wireless networks. Instead of treating probability distribution of reflection states as equiprobable (as scattering source of BackCom/SR) or degenerate (as reflecting element of RIS), UniScatter node adapts the input distribution of a passive scatterer based on link priority and Channel State Information (CSI), balancing information encoding and channel reconfiguration in a flexible and mutualistic manner. To accommodate signal characteristics, UniScatter receiver semi-coherently decodes all nodes from accumulated energy, determines equivalent primary channel over reflection pattern, then coherently decodes the primary link under enhanced multipath. It reduces the complexity of cooperative decoding while preserves the benefits of backscatter modulation and passive beamforming. Using shared spectrum, energy, and infrastructures, UniScatter is a general and powerful transmit-assist protocol that unifies BackCom, RIS and SR with universal hardware design and augmented Quality of Service (QoS) control. We consider an application scenario where a multi-antenna Access Point (AP) serves a single-antenna user surrounded by multiple UniScatter nodes, and characterize the achievable primary-total-backscatter rate region by designing input distribution at the nodes, active beamforming at the AP, and backscatter decision regions at the user. Simulation results demonstrate UniScatter nodes can flexibly control the transmit-assist tradeoff via smart input distribution design.

I. INTRODUCTION

FUTURE wireless network is envisioned to provide high throughput, uniform coverage, pervasive connectivity, heterogeneous control, and cognitive intelligence for trillions of portable devices. As an emerging low-power communication technique, Backscatter Communications (BackCom) separates conventional transmitter into a Radio-Frequency (RF) emitter with power-hungry elements (e.g., synthesizer and amplifier), and an information-bearing node with power-efficient components (e.g., harvester and modulator) [1]. The node harvests energy from emitted wave and embeds information over scattered

signal in a sustainable and controllable manner. The backscatter reader can be either co-located or separated with the emitter, known as monostatic and bistatic BackCom. Its applications such as Radio-Frequency Identification (RFID) [2], [3] and passive sensor network [4], [5] have been extensively researched, standardized, and commercialized to support Internet of Things (IoT) and Machine to Machine (M2M). However, traditional BackCom requires dedicated carrier emitter and backscatter reader, while passive nodes only respond when externally inquired. In Ambient Backscatter Communications (AmBC) [6], interactive nodes recycle ambient signals generated by legacy transmitters (e.g., radio, television, and Wi-Fi) to harvest energy and establish connection in between. It eliminates the need of dedicated power source, carrier emitter, and frequency spectrum, bringing more opportunities to low-power communications. To combat the strong direct-link interference of AmBC, [7] proposed a co-located receiver that cooperatively decodes the primary (legacy) and backscatter links. The authors evaluated the error performance of Maximum-Likelihood (ML), linear, and Successive Interference Cancellation (SIC) detectors for flat fading channel, and proposed a low-complexity detector for frequency-selective fading channel. The concept of cooperative AmBC was then refined as Symbiotic Radio (SR) to cognitively incorporate AmBC with existing systems [8]. In SR, the primary transmitter generates active radio carrying primary information, the secondary node modulates scattered component with backscatter information, and the cooperative receiver decodes both links from two propagation paths. The direct transmitter-receiver path only contains primary information, while the cascaded transmitter-node-receiver path preserves both thanks to signal characteristics. Such a coexistence was further classified into commensal, parasitic, and competitive relationships based on link priority [9], and their instantaneous rates, optimal power allocations, and outage probabilities were subsequently derived in [9], [10]. However, one important issue of SR is practical cooperative decoding design. Due to physical constraints at the load-switching modulator, backscatter symbol period is typically longer than primary. Ideal joint ML decoding achieves optimal performance with prohibitive computational complexity [7], [8], [11]. For sequential decoding from primary to backscatter, [12] pointed out the randomness from backscatter modulation can be modelled as either interference or channel uncertainty, depending on the symbol period ratio. The authors concluded if this ratio is sufficiently large, the non-coherent primary achievable rate would asymptotically approach its coherent counterpart. This motivated [7]–[17] to

The authors are with the Department of Electrical and Electronic Engineering, Imperial College London, London SW7 2AZ, U.K. (e-mail: {yang.zhao18, b.clerckx}@imperial.ac.uk).

first decode the primary link, perform SIC, then decode the backscatter link. However, the advantage of SIC is questionable because 1) sufficiently large symbol period ratio is assumed in primary rate analysis and constraints backscatter rate; 2) backscatter pattern and signal characteristics are not fully exploited; 3) non-coherent primary encoding is required at the transmitter, while re-encoding, precoding, and subtraction are required at the receiver; 4) primary and backscatter symbols are mixed by multiplication instead of superposition. Another open issue for SR is backscatter multiple access. [15] extended SIC to multi-node scenario and proposed a backscatter Non-Orthogonal Multiple Access (NOMA)-based SR with decoding order following backscatter signal strength. However, its performance deteriorates fast when the number of nodes increases. Backscatter Time-Division Multiple Access (TDMA) was also evaluated in [16], where each node transmits information during dedicated slot and harvests energy during others. It enhances energy efficiency by transmission time and reflection ratio optimization, but requires regular feedback to passive nodes and incurs high coordination cost. [18] controls the load-switching speed at nodes to shift the scattered signal to desired frequency bands. This enables backscatter Frequency-Division Multiple Access (FDMA) at the cost of extra bandwidth and higher power consumption. To reduce coordination between passive nodes, [17] proposed a random code-assisted multiple access for SR and evaluated the asymptotic Signal-to-Interference-plus-Noise Ratio (SINR) using random matrix theory. However, it suffers from imperfect synchronization and the near-far problem.

On the other hand, Reconfigurable Intelligent Surface (RIS) is a promising technology that evolves wireless propagation environment using numerous passive reflecting elements (e.g., scattering antenna or programmable metamaterial) with adjustable amplitudes and/or phases [19]. The scattered signals contain no additional information, but adds constructively or destructively with the direct component to enhance desired signal or suppress interference. Compared with backscatter nodes of BackCom/SR, RIS elements employ deterministic reflection pattern priorly known at transmitter and receiver. This motivated the use of fixed reflection coefficients during each channel block to improve communication, sensing, and power performances [20]–[25]. The concept of dynamic RIS, namely choosing independent reflection coefficients over different time slots within channel block, was first considered for resource blocks of Orthogonal Frequency-Division Multiplexing (OFDM) systems, then extended to power and information phases of Wireless Powered Communication Network (WPCN) [26]–[28]. Dynamic RIS provides artificial channel diversity and flexible resource allocation, but misses the opportunity to encode its own message. From an information-theoretic perspective, [29] reported using RIS as an auxiliary passive beamforming device to maximize the Signal-to-Noise Ratio (SNR) is generally rate-suboptimal for finite input constellations. Instead, joint transmitter-RIS encoding achieves the capacity of RIS-aided channel, and layered encoding with SIC decoding (i.e., SIC-based SR) can outperform pure passive beamforming at high SNR. It inspired [30]–[39] to employ RIS also as an information source to combine passive beamforming and backscatter modu-

lation in the overall reflection pattern. In particular, *symbol level precoding* maps backscatter symbols to RIS coefficient sets optimized for detection [30], [31], *overlay modulation* superposes information-bearing symbols over a common auxiliary matrix [32]–[35], *spatial modulation* switches between reflection coefficient sets that maximize SNR at different receive antennas [36]–[38], and *index modulation* divides RIS into reflection elements for passive beamforming and information elements for on-off modulation [39]. However, those RIS-empowered BackCom/SR designs involve advanced hardware architecture, high optimization complexity, and additional control overhead.

To the best of our knowledge, all relevant literatures assumed either Gaussian codebook [9], [10], [12]–[16], [34] or finite equiprobable inputs [7], [8], [11], [17], [30]–[33], [35]–[39] at backscatter information sources. The former is impractical for passive backscatter devices, while the latter does not fully exploit reflection pattern and Channel State Information (CSI). In this paper, we introduce UniScatter that generalizes Back-Com, SR, and RIS to manipulate the transmit-assist tradeoff via smart input distribution and backscatter detector design. The contributions of this paper are summarized as follows.

First, we propose UniScatter node to adapt the input probability distribution of a finite-state passive scatter device based on link priority and CSI. The reflection pattern over time is no longer fully random or deterministic, but can be flexibly distributed to unify and balance backscatter modulation with passive beamforming. Scattering source of BackCom/SR and reflecting element of RIS can be regarded as its extreme cases, where the input distribution boils down to equiprobable and degenerate, respectively. Like aforementioned RIS-empowered BackCom/SR schemes, the passive nodes require regular coordination with active devices, but the advantages are 1) UniScatter nodes can be built over conventional load-switching scatterers instead of composite metamaterial; 2) the optimization cost of input distribution is much lower than that of RIS reflection coefficients; 3) adaptive channel coding at backscatter sources can exploit CSI to achieve higher instantaneous rate than conventional uncoded transmission.

Second, we propose a practical receiving strategy that semi-coherently decodes all UniScatter messages from the received energy during each backscatter symbol block, re-encodes and re-covers their reflection patterns at each primary block, combines those with relevant CSI to construct equivalent primary channels, then coherently decodes the primary link under adapted multipath. The proposed receiver 1) preserves the benefits of backscatter modulation and passive beamforming; 2) enjoys lower computational and operational complexities than joint ML and SIC schemes; 3) accommodates the difference of symbol period in backscatter decoding; 4) exploits the reflection patterns in primary decoding; 5) suits for diverse symbol period ratios.

Third, we consider an application scenario where multiple UniScatter nodes ride over a point-to-point Multiple-Input Single-Output (MISO) transmission, performing backscatter modulation and passive beamforming to a nearby user using shared spectrum, energy, and infrastructures. To investigate how UniScatter unifies BackCom, SR and RIS for the benefits of both coexisting subsystems, we provide primary and backscatter rate analyses and emphasize the contributions of

input distribution at UniScatter nodes, active beamforming at the Access Point (AP), and backscatter decision regions at the user. This is the first paper to reveal the importance of those factors in RIS-empowered BackCom/SR.

Fourth, we characterize the achievable primary-total-backscatter rate region of the aforementioned system by optimizing the input distribution, active beamforming, and backscatter decision regions. It is formulated as a weighted sum-rate maximization subject to input probability simplex, average transmit power, and sequential decision threshold constraints. Since the original problem is highly non-convex, we decouple it into individual subproblems and constraint all decision regions to convex (connected) intervals. A suboptimal Block Coordinate Descent (BCD) algorithm is then proposed, where the Karush-Kuhn-Tucker (KKT) input distribution is numerically evaluated by limit of sequences, the active beamforming is iteratively updated by Projected Gradient Descent (PGD) accelerated by backtracking line search, and the decision regions are refined by existing thresholding designs.

Fifth, we provide numerical results to demonstrate the benefits of UniScatter and proposed algorithms. It is concluded that 1) UniScatter nodes provide flexible transmit-assist tradeoff using adaptive input distribution design; 2) when primary link is absolutely prioritized, the input probability of each node is 1 at one state and 0 at the others, which coincides with discretized RIS; 3) when backscatter link is absolutely prioritized, UniScatter nodes can exploit adaptive channel coding to achieve higher instantaneous rate than uncoded equiprobable transmission of BackCom/SR; 4) the proposed KKT input distribution design converges to stationary points, whose average performance is very close to global optimal; 5) the PGD beamforming achieves larger rate region than conventional Maximum Ratio Transmission (MRT); 6) the decision region schemes adapted to input distribution provide higher backscatter rates than the non-adaptive ML detector; 7) cooperation between passive nodes in terms of joint encoding can further boost the total backscatter rate; 8) the low complexity of input distribution design and the marginal effect of increasing reflection states motivates the use of low-order scatter nodes to replace high-resolution RIS.

Notations: Italic, bold lower-case, and bold upper-case letters denote scalars, vectors and matrices, respectively. $\mathbf{0}$ and $\mathbf{1}$ denote zero and one array of appropriate size, respectively. $\mathbb{R}_+^{x \times y}$ and $\mathbb{C}^{x \times y}$ denote the real nonnegative and complex spaces of dimension $x \times y$, respectively. j denotes the imaginary unit. $\mathrm{diag}(\cdot)$ returns a square matrix with the input vector on main diagonal. $(\cdot)^*$, $(\cdot)^T$, $(\cdot)^H$, $|\cdot|$, and $\|\cdot\|$ denote the conjugate, transpose, conjugate transpose, absolute value, and Euclidean norm operators, respectively. $(\cdot)^{(r)}$ and $(\cdot)^\star$ denote the r-th iterated and terminal solutions, respectively. The distribution of a Circularly Symmetric Complex Gaussian (CSCG) random variable with zero mean and variance σ^2 is denoted by $\mathcal{CN}(0,\sigma^2)$, and $\sim$ means "distributed as".

II. Scattering Principles

A. Scatterer Categories

Scattering refers to a change of moving direction of particles after colliding with others. It often involves *diffuse*

reflection where an incident ray is redistributed at many angles. An electromagnetic wave is scattered when an obstruction is placed in its propagation path. In RF applications such as BackCom, SR and RIS, the scatterer often includes *variable-load antenna* or *programmable metamaterial* with various reflection patterns [41].

1) Antenna-Based Scatterer: A typical antenna-based scatterer consists of an integrated antenna, a load-switching modulator, an energy harvester, and on-chip components (e.g., microcontroller and sensors) [2]. It first receives the impinging signals, then reradiates some back to the space and dissipates the remainder. According to transmission line theory, the scatter-absorb tradeoff depends on the impedance matching of the load and the antenna. For passive scatterers without dedicated energy source, a majority of incident wave is harvested to support node operation and the reradiated part can be relatively weak [42]. At the receiver, the observed signal can be further decomposed into *structural mode* and *antenna mode* components [43]. The former consistently contributes to environment multipath and is modelled within channel estimation, while the latter depends on impedance mismatch and can be used for backscatter modulation [1] and/or channel reconfiguration [41]. For antenna-based scatterers, the reflection coefficient at load state m is[1]

$$\Gamma_m = \frac{Z_m - Z_\mathrm{A}^*}{Z_m + Z_\mathrm{A}}, \tag{1}$$

where Z_m is the load impedance at state m and Z_A is the antenna input impedance.

2) Metamaterial-Based Scatterer: A typical metamaterial-based scatterer consists of multiple material layers and a smart controller [44]. The outer metamaterial layer involves numerous sub-wavelength structural units made of metallic or dielectric materials. The properties of unit cells can be artificially tuned for unconventional effective permittivity ϵ and permeability μ, producing customizable response to the electromagnetic field [45]. Using epsilon-negative material (e.g., conducing rods) or mu-negative material (e.g., split-ring resonators), ideal metamaterial-based scatterers can reflect the incident waves at the boundary between free space and metamaterial without receiving them [46]. This mainly applies a phase shift on the reflected wave and any propagation into the metamaterial would be evanescent. Depending on the type of metamaterial, its equivalent impedance can be controlled by voltage (for functional materials [47] and tunable diodes [48]) or architecture (for resonant elements [49]). For metamaterial-based scatterers with a discrete impedance set, the reflection coefficient at metamaterial state m is

$$\Gamma_m = \frac{Z_m - Z_0}{Z_m + Z_0}, \tag{2}$$

where Z_m is the equivalent impedance of metamaterial unit at state m and $Z_0 = 377\Omega$ is the characteristic impedance of free space.

B. BackCom/SR: Backscatter Modulation

BackCom and SR commonly employ antenna-based scatterers as passive information sources. By *frequently*

---

[1]It corresponds to a linear scatter model where the reflection coefficient is irrelevant to incident electromagnetic field strength.
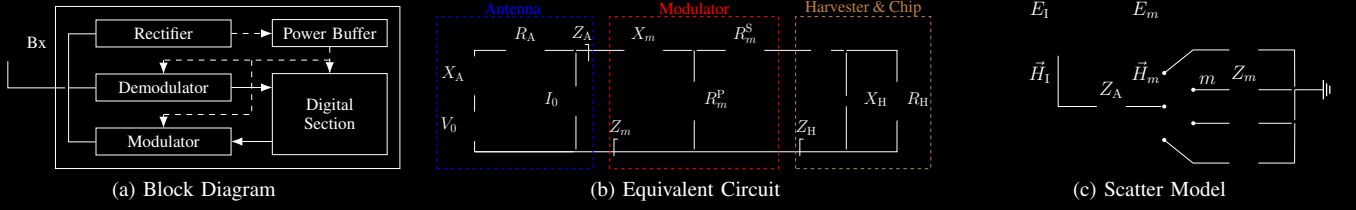
Fig. 1. Block diagram, equivalent circuit, and scatter model of a passive backscatter node. The solid and dashed vectors represent signal and energy flows. The backscatter antenna behaves as a constant power source, where the voltage V_0 and current I_0 are introduced by incident electric field $\vec{E}_I$ and magnetic field $\vec{H}_I$ [40].

switching between the available states, each backscatter node encodes self message over scattered signal and introduces backscatter uncertainty at the receiver. For M-ary Quadrature Amplitude Modulation (QAM), reflection coefficient Γ_m maps to the corresponding *complex constellation point* c_m by [42]

$$\Gamma_m = \alpha \frac{c_m}{\max_{m'} |c_{m'}|}, \qquad (3)$$

where $0 \leq \alpha \leq 1$ is the amplitude scattering ratio at the direction of interest.

C. RIS: Channel Reconfiguration

RIS typically involves a planar antenna array or metasurface of numerous metamaterial units as a passive channel reconfigurator. By *adaptively choosing* the reflection pattern, each reflecting element alters the phase of scattered signal for constructive/destructive superposition at the receiver. For each unit with M candidate states, reflection coefficient Γ_m maps to the corresponding *phase shift* θ_m by [20]

$$\Gamma_m = \beta_m \exp(j\theta_m), \qquad (4)$$

where $0 \leq \beta_m \leq 1$ is the overall amplitude scattering ratio of state m.

D. Opportunities

We have seen conventional scattering applications as BackCom, SR and RIS using the reflection pattern (1), (2) for either backscatter modulation (3) or passive beamforming (4). A natural but critical question is, for a given scatterer with pre-determined reflection pattern set, *can we softly bridge backscatter modulation and passive beamforming by appropriate reflection design?* This question is answered in Section III.

III. UniScatter

A. UniScatter Nodes

UniScatter nodes simultaneously transmit and assist by *adaptive input distribution design* based on primary and (cascaded) backscatter CSI. Instead of using fully random or deterministic reflection pattern over time, as shown in Fig. 2, UniScatter nodes semi-randomly select reflection state for each backscatter block, with *guidance of input probability* $P(\Gamma_m)$ for state m. In other words, it flexibly controls input distribution of candidate reflection states to balance backscatter encoding and passive beamforming.
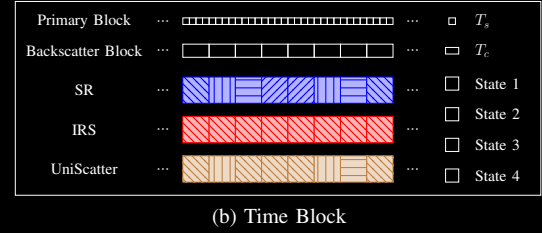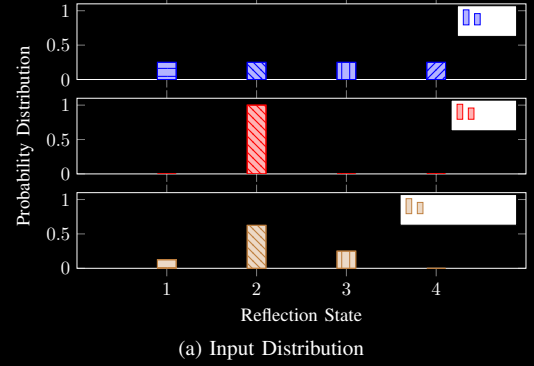

(a) Input Distribution

(b) Time Block

Fig. 2. Input probability distribution and time block structure of SR, RIS, and UniScatter. T_s and T_c respectively denote the primary and backscatter symbol period. Within channel coherence time, UniScatter nodes semi-randomly select reflection state for each backscatter block, with guidance from input probability distribution.
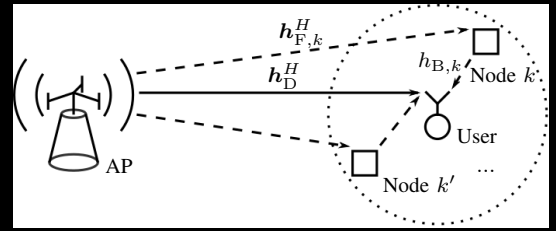

Fig. 3. A UniScatter-enabled single-user multi-node network.

Remark 1. *Compared to conventional RIS literatures that optimize phase shifts under unit-module constraint, UniScatter nodes start from predefined reflection coefficients and designs their input distribution under sum-probability constraint to achieve flexible primary-backscatter tradeoff.*

B. System Model

As shown in Fig. 3, we propose a UniScatter-enabled single-user multi-node MISO network where two coexisting systems share spectrum, energy and infrastructures. The primary point-to-point transmission from a Q-antenna AP to a single-antenna

user is assisted by K nearby single-antenna UniScatter nodes. In the secondary backscatter Multiple Access Channel (MAC) system, the AP serves as the carrier emitter, K nearby single-antenna UniScatter nodes modulate information over reradiated RF signals, and the user decodes their messages. For simplicity, we consider a quasi-static block fading model where channels remain constant within coherence interval while vary independently between consecutive blocks. Due to physical constraints on load switching, we assume the backscatter symbol period is $N \gg 1$ times longer than primary and consider integer N without loss of generality. We also assume the direct channel and all cascaded channels can be estimated and fed back to the AP.[2] Besides, we omit the signal reflected by two or more times [53] and ignore the time difference of arrival from different paths [9].

Denote the AP-user direct channel as $\boldsymbol{h}_{\mathrm{D}}^{H} \in \mathbb{C}^{1 \times Q}$, the AP-node $k \in \mathcal{K} \triangleq \{1,...,K\}$ forward channel as $\boldsymbol{h}_{\mathrm{F},k}^{H} \in \mathbb{C}^{1 \times Q}$, and the node k-user backward channel as $h_{\mathrm{B},k}$. Also, define the cascaded channel of tag k as $\boldsymbol{h}_{\mathrm{C},k}^{H} \triangleq h_{\mathrm{B},k} \boldsymbol{h}_{\mathrm{F},k}^{H} \in \mathbb{C}^{1 \times Q}$, and $\boldsymbol{H}_{\mathrm{C}} \triangleq [\boldsymbol{h}_{\mathrm{C},1},...,\boldsymbol{h}_{\mathrm{C},K}]^{H} \in \mathbb{C}^{K \times Q}$. Let $x_{\mathcal{K}} \triangleq (x_1,...,x_K)$ be the backscatter symbol tuple of all UniScatter nodes. Consider the signal model during one backscatter block (i.e., N primary blocks). Under perfect synchronization, the equivalent primary channel is a function of *coded* backscatter symbols

$$\boldsymbol{h}_{\mathrm{E}}^{H}(x_{\mathcal{K}}) \triangleq \boldsymbol{h}_{\mathrm{D}}^{H} + \sum_{k \in \mathcal{K}} \alpha_k \boldsymbol{h}_{\mathrm{C},k}^{H} x_k \tag{5a}$$

$$= \boldsymbol{h}_{\mathrm{D}}^{H} + \boldsymbol{x}^{H} \mathrm{diag}(\boldsymbol{\alpha}) \boldsymbol{H}_{\mathrm{C}}, \tag{5b}$$

where α_k is the amplitude scattering ratio of UniScatter node k, $\boldsymbol{\alpha} \triangleq [\alpha_1,...,\alpha_K]^T \in \mathbb{R}_+^{K \times 1}$, $x_k \in \mathcal{X} \triangleq \{c_1,...,c_M\}$ is the coded backscatter symbol of node k, and $\boldsymbol{x} \triangleq [x_1,...,x_K]^H \in \mathbb{C}^{K \times 1}$. The signal received by the user at primary block $n \in \mathcal{N} \triangleq \{1,...,N\}$ is

$$y[n] = \boldsymbol{h}_{\mathrm{E}}^{H}(x_{\mathcal{K}}) \boldsymbol{w} s[n] + v[n], \tag{6}$$

where $s \sim \mathcal{CN}(0,1)$ is the primary symbol, $v \sim \mathcal{CN}(0,\sigma_v^2)$ is the Additive White Gaussian Noise (AWGN), and $\boldsymbol{w} \in \mathbb{C}^{Q \times 1}$ is the active beamforming vector with average power constraint $\|\boldsymbol{w}\|^2 \leq P$.

Remark 2. *UniScatter involves a symbiotic MAC where the primary and backscatter symbols of different duration are mixed by Multiplication Coding (MC) instead of Superposition Coding (SC). For each node, the reflection coefficient not only encodes the backscatter message, but also influences the equivalent primary channel (5). To accommodate such signal characteristics, novel receiving strategy apart from SIC is desired to better utilize the reflection pattern and boost the primary-backscatter tradeoff.*

C. Receiving Strategy

We propose a UniScatter receiver where the backscatter messages of all UniScatter nodes are first jointly and semi-coherently detected using total received energy per backscatter
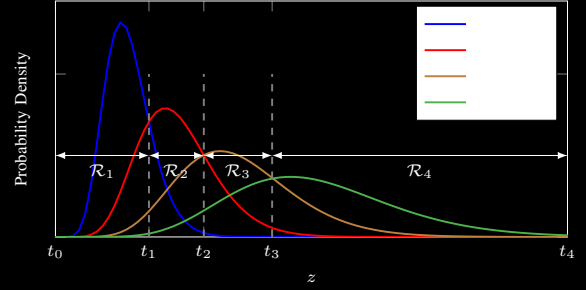
Fig. 4. PDF of total received energy per backscatter block, conditioned on different input hypothesis. Here, the convex ML decision regions are generally rate-suboptimal except for equiprobable inputs.

block, then modeled within equivalent channel (5) as dynamic passive beamforming. Compared with ML and SIC, UniScatter receiver allows practical and low-complexity node multiple access with minor adjustment over legacy equipments.

At a specific backscatter block, denote $m_k \in \mathcal{M}$ as the state index of node k, and let $m_{\mathcal{K}} \triangleq (m_1,...,m_K)$ be the state index tuple of all nodes. Conditioned on $m_{\mathcal{K}}$, the received signal at primary block n is subject to the variation of $s[n]$ and $v[n]$, distributed as $y[n] \sim \mathcal{CN}(0,\sigma_{m_{\mathcal{K}}}^2)$ with

$$\sigma_{m_{\mathcal{K}}}^2 = |\boldsymbol{h}_{\mathrm{E}}^{H}(x_{m_{\mathcal{K}}}) \boldsymbol{w}|^2 + \sigma_v^2, \tag{7}$$

where x_{m_k} and $x_{m_{\mathcal{K}}}$ are the symbol and symbol tuple associated with state m_k and state tuple $m_{\mathcal{K}}$, respectively.[3] Also, denote the total received energy within backscatter block as $z = \sum_{n=1}^{N} |y[n]|^2$. As the sum of N independent and identically distributed (i.i.d.) exponential variables, the Probability Density Function (PDF) of z conditioned on $m_{\mathcal{K}}$ follows Erlang distribution

$$f(z|\mathcal{H}_{m_{\mathcal{K}}}) = \frac{z^{N-1} \exp(-z/\sigma_{m_{\mathcal{K}}}^2)}{\sigma_{m_{\mathcal{K}}}^{2N} (N-1)!}, \tag{8}$$

where $\mathcal{H}_{m_{\mathcal{K}}}$ denotes hypothesis $m_{\mathcal{K}}$. To accommodate backscatter characteristics and reduce decoding complexity, we consider a joint semi-coherent detection for all UniScatter nodes over accumulated energy z. Once disjoint energy decision regions are determined, we can construct a Discrete Thresholding Multiple Access Channel (DTMAC) and formulate the transition probability from input $x_{m_{\mathcal{K}}}$ to output $\hat{x}_{m'_{\mathcal{K}}}$ as

$$P(\hat{x}_{m'_{\mathcal{K}}}|x_{m_{\mathcal{K}}}) = \int_{\mathcal{R}_{m'_{\mathcal{K}}}} f(z|\mathcal{H}_{m_{\mathcal{K}}}) dz, \tag{9}$$

where $\mathcal{R}_{m'_{\mathcal{K}}}$ is the decision region of hypothesis $\mathcal{H}_{m'_{\mathcal{K}}}$. An example of ML energy decision is illustrated in Fig. 4.

Remark 3. *The rate-optimal thresholding channel design remains under-investigated, and some attempts were made for single source with binary inputs in [54], [55]. For non-binary inputs with general distribution, the optimal decision region for each letter can be non-convex (i.e., with non-adjacent partitions) and the optimal number of thresholds is still unknown.*

In the following context, we restrict all decision regions to convex and optimize decision thresholds accordingly. That is, for any bijective mapping $f : m_{\mathcal{K}} \to \mathcal{L} \triangleq \{1,...,M^K\}$, the decision region of letter $l \in \mathcal{L}$ is defined as $\mathcal{R}_l \triangleq [t_{l-1}, t_l)$, where $t_{l-1} \leq t_l$. We also define the decision threshold vector as $\boldsymbol{t} \triangleq [t_0,...,t_L]^T \in \mathbb{R}_+^{(L+1)\times 1}$.

D. Achievable Rates

Denote the input probability of state m_k of UniScatter node k as $P_k(x_{m_k})$, and define the input probability distribution vector of node k as $\boldsymbol{p}_k \triangleq [P_k(c_1),...,P_k(c_M)]^T \in \mathbb{R}^{M\times 1}$. With independent encoding at all nodes, the probability of backscatter symbol tuple $x_{m_{\mathcal{K}}}$ is

$$P_{\mathcal{K}}(x_{m_{\mathcal{K}}}) = \prod_{k\in\mathcal{K}} P_k(x_{m_k}). \tag{10}$$

Similar to [56], we define the backscatter information function between input symbol tuple instance $x_{m_{\mathcal{K}}}$ and output symbol tuple $\hat{x}_{\mathcal{K}}$ as

$$I^{\mathrm{B}}(x_{m_{\mathcal{K}}}; \hat{x}_{\mathcal{K}}) \triangleq \sum_{m'_{\mathcal{K}}} P(\hat{x}_{m'_{\mathcal{K}}}|x_{m_{\mathcal{K}}}) \log \frac{P(\hat{x}_{m'_{\mathcal{K}}}|x_{m_{\mathcal{K}}})}{P(\hat{x}_{m'_{\mathcal{K}}})}, \tag{11}$$

where $P(\hat{x}_{m'_{\mathcal{K}}}) = \sum_{m_{\mathcal{K}}} P_{\mathcal{K}}(x_{m_{\mathcal{K}}})P(\hat{x}_{m'_{\mathcal{K}}}|x_{m_{\mathcal{K}}})$. We also define the backscatter marginal information of letter x_{m_k} of node k as

$$I_k^{\mathrm{B}}(x_{m_k}; \hat{x}_{\mathcal{K}}) \triangleq \sum_{m_{\mathcal{K}\setminus\{k\}}} P_{\mathcal{K}\setminus\{k\}}(x_{m_{\mathcal{K}\setminus\{k\}}}) I^{\mathrm{B}}(x_{m_{\mathcal{K}}}; \hat{x}_{\mathcal{K}}), \tag{12}$$

where $P_{\mathcal{K}\setminus\{k\}}(x_{m_{\mathcal{K}\setminus\{k\}}}) = \prod_{q\in\mathcal{K}\setminus\{k\}} P_q(x_{m_q})$. Moreover, we can write the backscatter mutual information as

$$I^{\mathrm{B}}(x_{\mathcal{K}}; \hat{x}_{\mathcal{K}}) = \sum_{m_{\mathcal{K}}} P_{\mathcal{K}}(x_{m_{\mathcal{K}}}) I^{\mathrm{B}}(x_{m_{\mathcal{K}}}; \hat{x}_{\mathcal{K}}). \tag{13}$$

Once backscatter messages are successfully decoded, we can re-encode to determine $x_{\mathcal{K}}$ and retrieve equivalent primary channel by (5). We define the primary information function conditioned on backscatter symbol tuple $x_{m_{\mathcal{K}}}$ as

$$I^{\mathrm{P}}(s;y|x_{m_{\mathcal{K}}}) \triangleq \log\left(1 + \frac{|\boldsymbol{h}_{\mathrm{E}}^H(x_{m_{\mathcal{K}}})\boldsymbol{w}|^2}{\sigma_v^2}\right), \tag{14}$$

the primary marginal information conditioned on letter x_{m_k} of node k as

$$I_k^{\mathrm{P}}(s;y|x_{m_k}) \triangleq \sum_{m_{\mathcal{K}\setminus\{k\}}} P_{\mathcal{K}\setminus\{k\}}(x_{m_{\mathcal{K}\setminus\{k\}}}) I^{\mathrm{P}}(s;y|x_{m_{\mathcal{K}}}), \tag{15}$$

and the primary ergodic mutual information as

$$I^{\mathrm{P}}(s;y|x_{\mathcal{K}}) = \sum_{m_{\mathcal{K}}} P_{\mathcal{K}}(x_{m_{\mathcal{K}}}) I^{\mathrm{P}}(s;y|x_{m_{\mathcal{K}}}). \tag{16}$$

Finally, with a slight abuse of notation, we define the corresponding weighted sum information function, marginal information, and mutual information respectively as

$$I(x_{m_{\mathcal{K}}}) \triangleq \rho I^{\mathrm{P}}(s;y|x_{m_{\mathcal{K}}}) + (1-\rho) I^{\mathrm{B}}(x_{m_{\mathcal{K}}}; \hat{x}_{\mathcal{K}}), \tag{17}$$

$$I_k(x_{m_k}) \triangleq \rho I_k^{\mathrm{P}}(s;y|x_{m_k}) + (1-\rho) I_k^{\mathrm{B}}(x_{m_k}; \hat{x}_{\mathcal{K}}), \tag{18}$$

$$I(x_{\mathcal{K}}) \triangleq \rho I^{\mathrm{P}}(s;y|x_{\mathcal{K}}) + (1-\rho) I^{\mathrm{B}}(x_{\mathcal{K}}; \hat{x}_{\mathcal{K}}), \tag{19}$$

where $0 \leq \rho \leq 1$ is the relative priority of the primary link.

IV. INPUT DISTRIBUTION, ACTIVE BEAMFORMING, AND DECISION THRESHOLD DESIGN

To characterize the achievable primary-total-backscatter rate region of the proposed UniScatter-enabled network, we aim to maximize the weighted sum mutual information with respect to node input distributions $\{\boldsymbol{p}_k\}_{k\in\mathcal{K}}$, active beamforming vector $\boldsymbol{w}$, and decision threshold vector $\boldsymbol{t}$ as

$$\max_{\{\boldsymbol{p}_k\}_{k\in\mathcal{K}}, \boldsymbol{w}, \boldsymbol{t}\in\mathbb{R}_+^{L+1}} I(x_{\mathcal{K}}) \tag{20a}$$

$$\text{s.t.} \quad \sum_{m_k} P_k(x_{m_k}) = 1, \quad \forall k, \tag{20b}$$

$$P_k(x_{m_k}) \geq 0, \quad \forall k, m_k, \tag{20c}$$

$$\|\boldsymbol{w}\|^2 \leq P, \tag{20d}$$

$$t_{l-1} \leq t_l, \quad \forall l. \tag{20e}$$

Problem (20) is highly non-convex, and we propose a BCD algorithm that iteratively updates $\{\boldsymbol{p}_k\}_{k\in\mathcal{K}}$, $\boldsymbol{w}$ and $\boldsymbol{t}$ until convergence.

A. Input Distribution

For any given $\boldsymbol{w}$ and $\boldsymbol{t}$, we can construct the equivalent DTMAC by (9) and simplify (20) to

$$\max_{\{\boldsymbol{p}_k\}_{k\in\mathcal{K}}} I(x_{\mathcal{K}}) \tag{21a}$$

$$\text{s.t.} \quad (20b),(20c), \tag{21b}$$

which involves coupled term $\prod_{k\in\mathcal{K}} P_k(x_{m_k})$ and is non-convex when $K > 1$. Next, we propose a numerical method that evaluate the KKT input distribution by limit of sequences.

Remark 4. *As pointed out in [57], KKT conditions are generally necessary but insufficient for total rate maximization in discrete memoryless MAC. Therefore, KKT solutions may end up being saddle points of problem* (21).

Following [56], we first recast KKT conditions to their equivalent form for problem (21), then propose an iterative method that guarantees input distribution satisfying above conditions on convergence.

Proposition 1. *The KKT optimality conditions for problem* (21) *are equivalent to,* $\forall k, m_k,$

$$I_k^{\star}(x_{m_k}) = I^{\star}(x_{\mathcal{K}}), \quad P_k^{\star}(x_{m_k}) > 0, \tag{22a}$$

$$I_k^{\star}(x_{m_k}) \leq I^{\star}(x_{\mathcal{K}}), \quad P_k^{\star}(x_{m_k}) = 0. \tag{22b}$$

Proof. Please refer to Appendix A. $\square$

For each node, (22a) suggests each probable state should produce the same marginal information (averaged over all states of other nodes), while (22b) implies any state with potentially less marginal information should not be used.

Proposition 2. *The KKT input probability of node k of state m_k is given by the converging point of the sequence*

$$P_k^{(r+1)}(x_{m_k}) = \frac{P_k^{(r)}(x_{m_k})\exp\left(\frac{\rho}{1-\rho}I_k^{(r)}(x_{m_k})\right)}{\sum_{m'_k} P_k^{(r)}(x_{m'_k})\exp\left(\frac{\rho}{1-\rho}I_k^{(r)}(x_{m'_k})\right)}, \tag{23}$$

Algorithm 1: Numerical Evaluation of KKT Input Distribution

Input: K, N, $\boldsymbol{h}_{\mathrm{D}}^{H}$, $\boldsymbol{H}_{\mathrm{C}}$, $\boldsymbol{\alpha}$, $\mathcal{X}$, σ_v^2, ρ, $\boldsymbol{w}$, $\boldsymbol{t}$, ϵ
Output: $\{\boldsymbol{p}_k^\star\}_{k\in\mathcal{K}}$
1: Set $\boldsymbol{h}_{\mathrm{E}}^{H}(x_{m_\mathcal{K}})$, $\forall m_\mathcal{K}$ by (5)
2:      $\sigma_{m_\mathcal{K}}^2$, $\forall m_\mathcal{K}$ by (7)
3:      $f(z|\mathcal{H}_{m_\mathcal{K}})$, $\forall m_\mathcal{K}$ by (8)
4:      $P(\hat{x}_{m'_\mathcal{K}}|x_{m_\mathcal{K}})$, $\forall m_\mathcal{K}, m'_\mathcal{K}$ by (9)
5: Initialize $r \leftarrow 0$
6:      $\boldsymbol{p}_k^{(0)} > \boldsymbol{0}$, $\forall k$
7: Get $P_\mathcal{K}^{(r)}(x_{m_\mathcal{K}})$, $\forall m_\mathcal{K}$ by (10)
8:      $I^{(r)}(x_{m_\mathcal{K}})$, $\forall m_\mathcal{K}$ by (11), (14), (17)
9:      $I_k^{(r)}(x_{m_k})$, $\forall k, m_k$ by (12), (15), (18)
10:      $I^{(r)}(x_\mathcal{K})$ by (13), (16), (19)
11: **Repeat**
12:      Update $r \leftarrow r+1$
13:          $\boldsymbol{p}_k^{(r)}$, $\forall k$ by (23)
14:      Redo step 7–10
15: **Until** $I^{(r)}(x_\mathcal{K}) - I^{(r-1)}(x_\mathcal{K}) \le \epsilon$

Algorithm 2: Iterative Active Beamforming Design by PGD with Backtracking Line Search

Input: Q, N, $\boldsymbol{h}_{\mathrm{D}}^{H}$, $\boldsymbol{H}_{\mathrm{C}}$, $\boldsymbol{\alpha}$, $\mathcal{X}$, P, σ_v^2, ρ, $\{\boldsymbol{p}_k\}_{k\in\mathcal{K}}$, $\boldsymbol{t}$, α, β, γ, ϵ
Output: $\boldsymbol{w}^\star$
1: Set $\boldsymbol{h}_{\mathrm{E}}^{H}(x_{m_\mathcal{K}})$, $\forall m_\mathcal{K}$ by (5)
2:      $P_\mathcal{K}(x_{m_\mathcal{K}})$, $\forall m_\mathcal{K}$ by (10)
3: Initialize $r \leftarrow 0$
4:      $\boldsymbol{w}^{(0)}$, $\|\boldsymbol{w}^{(0)}\|^2 \le P$
5: Get $(\sigma_{m_\mathcal{K}}^{(r)})^2$, $\forall m_\mathcal{K}$ by (7)
6:      $Q^{(r)}\big(N, \frac{t_{l-1}}{\sigma_{m_\mathcal{K}}^2}, \frac{t_l}{\sigma_{m_\mathcal{K}}^2}\big)$, $\forall m_\mathcal{K}, l$ by (26) or (27)
7:      $I^{(r)}(x_\mathcal{K})$ by (25)
8:      $\nabla_{\boldsymbol{w}^*} Q^{(r)}\big(N, \frac{t_{l-1}}{\sigma_{m_\mathcal{K}}^2}, \frac{t_l}{\sigma_{m_\mathcal{K}}^2}\big)$, $\forall m_\mathcal{K}, l$ by (28)
9:      $\nabla_{\boldsymbol{w}^*} I^{(r)}(x_\mathcal{K})$ by (29)
10: **Repeat**
11:      Update $r \leftarrow r+1$
12:          $\gamma^{(r)} \leftarrow \gamma$
13:          $\bar{\boldsymbol{w}}^{(r)} \leftarrow \boldsymbol{w}^{(r-1)} + \gamma \nabla_{\boldsymbol{w}^*} I^{(r-1)}(x_\mathcal{K})$
14:          $\boldsymbol{w}^{(r)}$ by (30)
15:      Redo step 5–7
16:      **While** $I^{(r)}(x_\mathcal{K}) < I^{(r-1)}(x_\mathcal{K}) + \alpha\gamma\|\nabla_{\boldsymbol{w}^*} I^{(r-1)}(x_\mathcal{K})\|^2$
17:          Set $\gamma^{(r)} \leftarrow \beta\gamma^{(r)}$
18:          Redo step 13–15
19:      **End While**
20:      Redo step 8, 9
21: **Until** $\|\boldsymbol{w}^{(r)} - \boldsymbol{w}^{(r-1)}\| \le \epsilon$

---

where r is the iteration index and $\boldsymbol{p}_k^{(0)} > \boldsymbol{0}$, $\forall k$.

Proof. Please refer to Appendix B. □

At each iteration, the input distribution of node k is evaluated over updated input distribution of node 1 to $k-1$, together with previous input distribution of node $k+1$ to K. The KKT input distribution design is summarized in Algorithm 1.

B. Active Beamforming

For any given $\{\boldsymbol{p}_k\}_{k\in\mathcal{K}}$ and $\boldsymbol{t}$, problem (20) reduces to

$$\max_{\boldsymbol{w}} \quad I(x_\mathcal{K}) \tag{24a}$$

$$\text{s.t.} \quad (20\text{d}), \tag{24b}$$

which is still non-convex due to integration and entropy terms. To see this, we explicitly write (24a) as (25) at the bottom of page 7, where

$$Q\Big(N, \frac{t_{l-1}}{\sigma_{m_\mathcal{K}}^2}, \frac{t_l}{\sigma_{m_\mathcal{K}}^2}\Big) = \frac{\int_{t_{l-1}/\sigma_{m_\mathcal{K}}^2}^{t_l/\sigma_{m_\mathcal{K}}^2} z^{N-1}\exp(-z)dz}{(N-1)!} \tag{26}$$

is the regularized incomplete Gamma function that substitutes the DTMAC transition probability (9). Its series representation is given by [58, Theorem 3]

$$Q\Big(N, \frac{t_{l-1}}{\sigma_{m_\mathcal{K}}^2}, \frac{t_l}{\sigma_{m_\mathcal{K}}^2}\Big) = \exp\Big(-\frac{t_{l-1}}{\sigma_{m_\mathcal{K}}^2}\Big) \sum_{n=0}^{N-1} \frac{\big(\frac{t_{l-1}}{\sigma_{m_\mathcal{K}}^2}\big)^n}{n!}$$
$$- \exp\Big(-\frac{t_l}{\sigma_{m_\mathcal{K}}^2}\Big) \sum_{n=0}^{N-1} \frac{\big(\frac{t_l}{\sigma_{m_\mathcal{K}}^2}\big)^n}{n!}. \tag{27}$$

Next, we derive the gradients of (27) and (25) w.r.t. $\boldsymbol{w}^*$ as (28) and (29) at the end of page 8 and 8, respectively. It allows problem (24) to be solved by the PGD method, where any unregulated beamforming vector $\bar{\boldsymbol{w}}$ can be projected onto the feasible domain of average transmit power constraint (20d) by

$$\boldsymbol{w} = \sqrt{P}\frac{\bar{\boldsymbol{w}}}{\max\big(\sqrt{P}, \|\bar{\boldsymbol{w}}\|\big)}. \tag{30}$$

We present the iterative active beamforming design accelerated by backtracking line search in Algorithm 2.

C. Decision Threshold

For any given $\{\boldsymbol{p}_k\}_{k\in\mathcal{K}}$ and $\boldsymbol{w}$, problem (20) reduces to

$$\max_{\boldsymbol{t}\in\mathbb{R}_+^{L+1}} \quad I(x_\mathcal{K}) \tag{31a}$$

$$\text{s.t.} \quad (20\text{e}), \tag{31b}$$

where it is trivial to conclude $t_0^\star = 0$ and $t_L^\star = \infty$ for energy-based backscatter detection.

Remark 5. *Backscatter detection (and decision design) has no impact on primary achievable rate. When nodes transmit at non-zero total rate, the user can re-encode backscatter messages to*

$$I(x_\mathcal{K}) = \sum_{m_\mathcal{K}} P_\mathcal{K}(x_{m_\mathcal{K}}) \Bigg(\rho\log\Big(1 + \frac{|\boldsymbol{h}_{\mathrm{E}}^{H}(x_{m_\mathcal{K}})\boldsymbol{w}|^2}{\sigma_v^2}\Big) + (1-\rho)\sum_l Q\Big(N, \frac{t_{l-1}}{\sigma_{m_\mathcal{K}}^2}, \frac{t_l}{\sigma_{m_\mathcal{K}}^2}\Big) \log\frac{Q\Big(N, \frac{t_{l-1}}{\sigma_{m_\mathcal{K}}^2}, \frac{t_l}{\sigma_{m_\mathcal{K}}^2}\Big)}{\sum_{m'_\mathcal{K}} P_\mathcal{K}(x_{m'_\mathcal{K}})Q\Big(N, \frac{t_{l-1}}{\sigma_{m'_\mathcal{K}}^2}, \frac{t_l}{\sigma_{m'_\mathcal{K}}^2}\Big)} \Bigg) \tag{25}$$

recover coded backscatter tuple $x_\mathcal{K}$ at each block. Otherwise, $x_\mathcal{K}$ can be fully deterministic and known to the user.

Remark 5 suggests any t maximizes total backscatter mutual information $I^B(x_\mathcal{K};\hat{x}_\mathcal{K})$ is also optimal for problem (31).

Remark 6. *In terms of total backscatter rate, the nodes can be regarded as an equivalent source with augmented alphabet of symbol tuple $x_{m_\mathcal{K}}$, and the DTMAC (9) essentially reduces to a Discrete Memoryless Thresholding Channel (DMTC).*

Finally, we can employ existing thresholding design for DMTC to solve problem (31). For example, [59] first discretized the continuous energy z into numerous output bins, then grouped adjacent bins to maximize mutual information using Dynamic Programming (DP) accelerated by Shor-Moran-Aggarwal-Wilber-Klawe (SMAWK) algorithm. In [60], the authors first proved the optimality condition for any three neighbor thresholds, then fix t_0, traverse t_1, and sequentially optimizes the others by bisection. Both will be compared with ML decision [61]

$$t_l^{\mathrm{ML}} = N \frac{\sigma_{l-1}^2 \sigma_l^2}{\sigma_{l-1}^2 - \sigma_l^2} \log \frac{\sigma_{l-1}^2}{\sigma_l^2}, \quad l \in \mathcal{L} \setminus \{0, L\}, \qquad (32)$$

which is generally suboptimal for problem (31) except for equiprobable inputs at all nodes.

V. SIMULATION RESULTS

In this section, we provide numerical results to evaluate the proposed input, beamforming and decision design over a single-user multi-node UniScatter-enabled network. We assume the distance between AP and user is $10\,\mathrm{m}$, and $K = 2$ UniScatter nodes are uniformly dropped within a disk centered at the user of radius $1\,\mathrm{m}$. The carrier frequency is $f = 200\mathrm{MHz}$, and we consider i.i.d. Ricean fading between all terminals. For direct, forward and backward links, we set the

path loss exponents to 2.6, 2.4 and 2, and the Ricean factor to 5, 5 and 10, respectively. The AP has $Q = 4$ antennas with maximum average transmit power $P = 36\mathrm{dBm}$. All nodes have amplitude scattering ratio $\alpha = 0.5$, symbol period ratio $N = 20$, and perform QAM with $M = 4$ input states. The user is with average noise power $\sigma_v^2 = 70\mathrm{dBm}$ and receive antenna gain $3\,\mathrm{dBi}$. All rate regions are averaged over at least 1000 instances, where "PSP" and "BSP" means primary and backscatter symbol periods, respectively. We choose decision design by SMAWK [59] as reference, and select discretize boundaries uniformly over the 95% confidence region of edge hypotheses. The parameters remain fixed unless otherwise specified.

A. Input Distribution vs. Weight

In Fig. 5, we present typical input distributions of a single UniScatter node with $M = 4$ inputs under different weight ρ. Fig. 5(a) and 5(b) are obtained from i.i.d. drop and channel realizations. We note that even for $\rho = 0$ (i.e., best backscatter performance), the optimal input distribution is not equiprobable like SR, and adaptive channel coding can further increase total backscatter rate based on CSI. On the other hand, the optimal input distribution becomes fully deterministic at $\rho = 1$ (i.e., best primary performance), where the state maximizes equivalent primary channel (5) strength is chosen with probability 1. In this case, UniScatter node boils down to a RIS element with M discrete states. As ρ moves from 0 to 1, the optimal input distribution becomes gradually biased to one state and flexibly balances the primary-backscatter tradeoff.

B. Rate Region vs. Input, Beamforming, and Decision Schemes

Fig. 6(a) compares the achievable rate regions by following input designs.

- **Exhaustion:** K-dimensional grid search over probability simplex;

$$\nabla_{\boldsymbol{w}^*} Q\left(N, \frac{t_{l-1}}{\sigma_{m_\mathcal{K}}^2}, \frac{t_l}{\sigma_{m_\mathcal{K}}^2}\right) = \frac{\boldsymbol{h}_\mathrm{E}(x_{m_\mathcal{K}}) \boldsymbol{h}_\mathrm{E}^H(x_{m_\mathcal{K}}) \boldsymbol{w}}{\left(|\boldsymbol{h}_\mathrm{E}^H(x_{m_\mathcal{K}}) \boldsymbol{w}|^2 + \sigma_v^2\right)^2}$$

$$\times \left(t_l \exp\left(-\frac{t_l}{|\boldsymbol{h}_\mathrm{E}^H(x_{m_\mathcal{K}})\boldsymbol{w}|^2 + \sigma_v^2}\right)\left(-1 + \sum_{n=1}^{N-1} \frac{n\left(\frac{t_l}{|\boldsymbol{h}_\mathrm{E}^H(x_{m_\mathcal{K}})\boldsymbol{w}|^2 + \sigma_v^2}\right)^{n-1} - \left(\frac{t_l}{|\boldsymbol{h}_\mathrm{E}^H(x_{m_\mathcal{K}})\boldsymbol{w}|^2 + \sigma_v^2}\right)^n}{n!}\right)\right.$$

$$\left. - t_{l-1} \exp\left(-\frac{t_{l-1}}{|\boldsymbol{h}_\mathrm{E}^H(x_{m_\mathcal{K}})\boldsymbol{w}|^2 + \sigma_v^2}\right)\left(-1 + \sum_{n=1}^{N-1} \frac{n\left(\frac{t_{l-1}}{|\boldsymbol{h}_\mathrm{E}^H(x_{m_\mathcal{K}})\boldsymbol{w}|^2 + \sigma_v^2}\right)^{n-1} - \left(\frac{t_{l-1}}{|\boldsymbol{h}_\mathrm{E}^H(x_{m_\mathcal{K}})\boldsymbol{w}|^2 + \sigma_v^2}\right)^n}{n!}\right)\right) \qquad (28)$$

$$\nabla_{\boldsymbol{w}^*} I(x_\mathcal{K}) = \sum_{m_\mathcal{K}} P_\mathcal{K}(x_{m_\mathcal{K}}) \left(\rho \frac{\boldsymbol{h}_\mathrm{E}(x_{m_\mathcal{K}}) \boldsymbol{h}_\mathrm{E}^H(x_{m_\mathcal{K}}) \boldsymbol{w}}{|\boldsymbol{h}_\mathrm{E}^H(x_{m_\mathcal{K}})\boldsymbol{w}|^2 + \sigma_v^2} + (1-\rho) \sum_l \left(\log \frac{Q\left(N, \frac{t_{l-1}}{\sigma_{m_\mathcal{K}}^2}, \frac{t_l}{\sigma_{m_\mathcal{K}}^2}\right)}{\sum_{m'_\mathcal{K}} P_\mathcal{K}(x_{m'_\mathcal{K}}) Q\left(N, \frac{t_{l-1}}{\sigma_{m'_\mathcal{K}}^2}, \frac{t_l}{\sigma_{m'_\mathcal{K}}^2}\right)} + 1\right)\right.$$

$$\left. \times \nabla_{\boldsymbol{w}^*} Q\left(N, \frac{t_{l-1}}{\sigma_{m_\mathcal{K}}^2}, \frac{t_l}{\sigma_{m_\mathcal{K}}^2}\right) - \frac{Q\left(N, \frac{t_{l-1}}{\sigma_{m_\mathcal{K}}^2}, \frac{t_l}{\sigma_{m_\mathcal{K}}^2}\right) \sum_{m'_\mathcal{K}} P_\mathcal{K}(x_{m'_\mathcal{K}}) \nabla_{\boldsymbol{w}^*} Q\left(N, \frac{t_{l-1}}{\sigma_{m'_\mathcal{K}}^2}, \frac{t_l}{\sigma_{m'_\mathcal{K}}^2}\right)}{\sum_{m'_\mathcal{K}} P_\mathcal{K}(x_{m'_\mathcal{K}}) Q\left(N, \frac{t_{l-1}}{\sigma_{m'_\mathcal{K}}^2}, \frac{t_l}{\sigma_{m'_\mathcal{K}}^2}\right)}\right) \qquad (29)$$

(a) Instance 1   (b) Instance 2
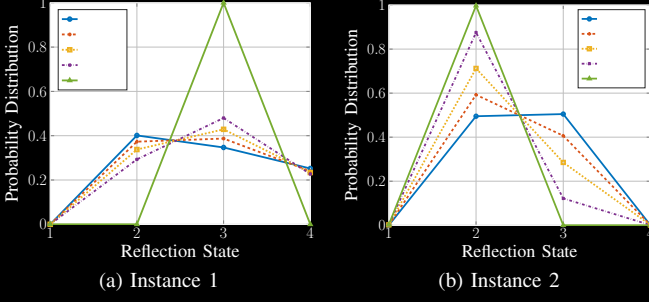
Fig. 5. Typical input distributions vs. weight ρ for a UniScatter node with $M = 4$ inputs.

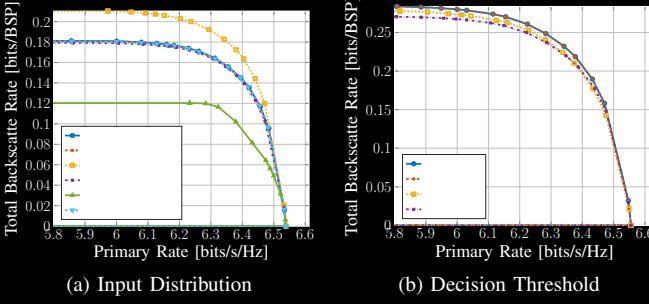(a) Input Distribution   (b) Decision Threshold

Fig. 6. Average primary-total-backscatter rate regions for different input distribution and decision threshold schemes.

- **KKT:** results of Algorithm 1;
- **Cooperation:** backscatter cooperation/joint encoding at all UniScatter nodes, tuple input distribution/joint probability array optimization by Blahut-Arimoto algorithm [62], [63];
- **Marginalization:** marginal distributions of joint probability array;
- **Decomposition:** normalized tensors of rank-1 Canonical Polyadic (CP) decomposition of joint probability array;
- **Randomization:** Gaussian recovery from joint probability array [64].

We notice adaptive joint encoding at all nodes provides the outer bound of rate region. However, it involves arbitrarily dependent codewords, and backscatter cooperation between passive nodes is generally unaffordable. In contrast, the rate region of KKT input design in Algorithm 1 approaches that of exhaustive search, and the loss is negligible for $K = 2$. Although the randomization method [64] returns similar rate region, it requires solving $K + 1$ linear programming problems before applying Gaussian recovery. The marginal distribution is slightly worse than KKT despite having the same computational complexity, while the approximation from CP decomposition is unsatisfying.

Fig. 6(b) compares the achievable rate region by following threshold schemes.

- **DP:** sequential quantizer grouping by dynamic programming [59];
- **SMAWK:** above accelerated by SMAWK algorithm;
- **Bisection:** sequential bisection threshold design [60];
- **ML:** maximum likelihood decision (32) [61].

We observe that input distribution-adaptive threshold designs

(a) Metscatter Nodes   (b) Input States

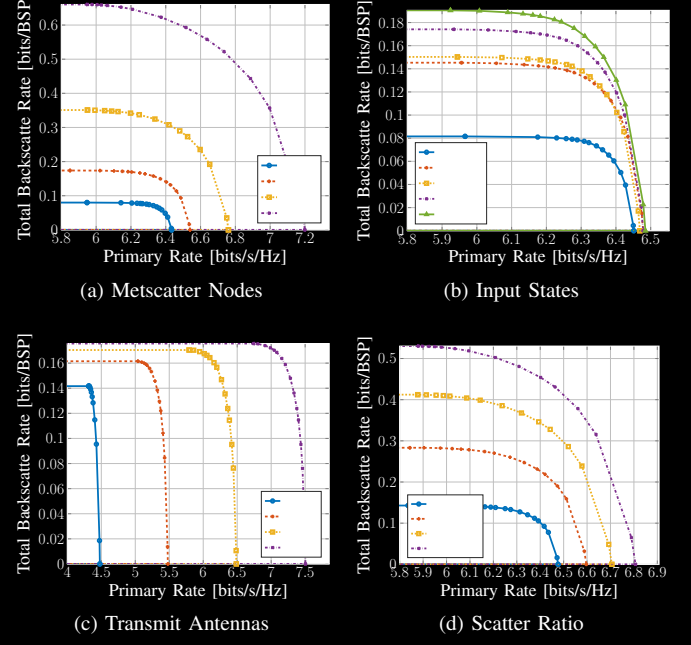(c) Transmit Antennas   (d) Scatter Ratio

Fig. 7. Average primary-total-backscatter rate regions.

achieve higher total backscatter rate than ML. This is because the decision regions can be flexibly adjusted to enhance the capacity of DTMAC (9). For example, the tuples with negligible input probability should have narrower decision regions than those frequently employed, in order to improve detection performance. It emphasizes the importance of joint input distribution and decision region design.

C. Rate Region vs. System Configuration

We present in 7 the impact of UniScatter nodes, input states, transmit antennas and scatter ratio on the achievable rate region. For the specified scenario, Fig. 7(a) shows the total backscatter rate almost scales proportionally with the number of UniScatter nodes, and the decrease of individual backscatter rate is unobvious. Besides, we conclude from 7(b) that increasing the reflection states has a marginal effect on both primary and backscatter rates. Those two facts motivates the use of numerous elementary/uncomplicated backscatter nodes, instead of high-order transponders or programmable high-resolution surfaces. Figs. 7(c) and 7(d) also prove increasing transmit antennas or scatter ratio can improve both primary and backscatter performance.

Fig. 8(a) shows the tradeoff between coverage disk radius r and achievable rate region. When nodes are far from the user, both primary and backscatter rates decrease due to the product pass loss of forward and backward channels. Under the assumption of ideal backscatter decoding and re-encoding, Fig. 8(b) suggests using lower symbol period ratio N can boost total backscatter rate per primary symbol. However, it requires more frequent detection and re-encoding at the user to maintain the primary rate. When N becomes sufficiently large, total backscatter rate approaches 0 and UniScatter nodes boil down to conventional RIS elements with fixed reflection pattern during whole channel block. In Fig. 8(c), we observe

(a) Node Coverage

(b) Symbol Period Ratio

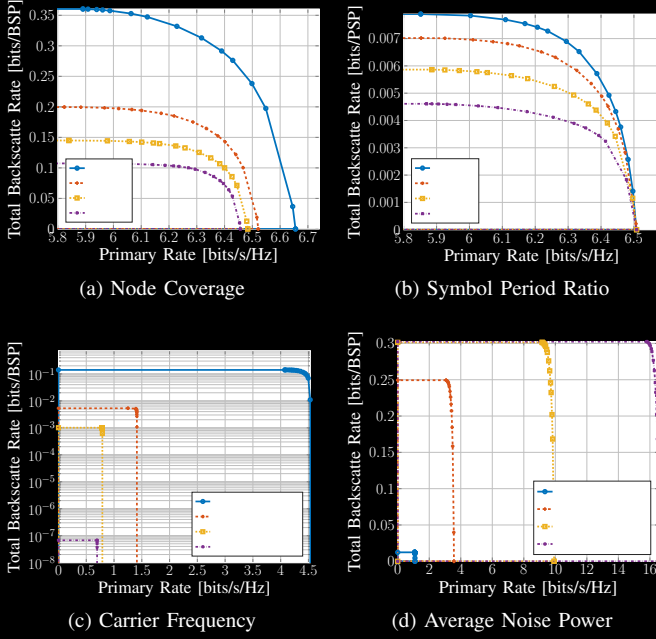(c) Carrier Frequency

(d) Average Noise Power

Fig. 8. Average primary-total-backscatter rate regions.

that passive UniScatter nodes achieve higher backscatter rate at lower carrier frequency because of preferable propagation loss. Finally, 8(d) prove the performance of energy detection is robust for a wide range of noise power.

VI. CONCLUSION

This paper introduced UniScatter that adapts input distribution of passive backscatter nodes to simultaneously transmit and assist over existing wireless systems. Starting from backscatter principles, we showed how UniScatter nodes bridges and generalizes parasitic source of SR and reflecting element of RIS via smart input design. An application scenario was considered where multiple UniScatter nodes ride over a point-to-point transmission to simultaneously encode self message and perform passive beamforming. To characterize achievable primary-backscatter rate region, we proposed a BCD algorithm that evaluates KKT input distribution in closed form, optimizes active beamforming by PGD, and refines decision regions by existing methods. Numerical results demonstrated the advantage of adaptive node input distribution design for both primary and backscatter subsystems.

One particular interesting question is how to design UniScatter node and receiver in a multi-user system. If one node can contribute to and be decoded by multiple users, its input distribution may be further adjusted to mimic multi-beam gain of dynamic beamforming [65].

APPENDIX

A. Proof of Proposition 1

Denote the Lagrange multipliers associated with (20b) and (20c) as $\{\nu_k\}_{k\in\mathcal{K}}$ and $\{\lambda_{k,m_k}\}_{k\in\mathcal{K},m_k\in\mathcal{M}}$, respectively. The

Lagrangian function of problem (21) is

$$L=-I(x_\mathcal{K})+\sum_k\nu_k\left(\sum_{m_k\in\mathcal{M}}P_k(x_{m_k})-1\right)$$
$$-\sum_k\sum_{m_k}\lambda_{k,m_k}P_k(x_{m_k}),\tag{33}$$

and the KKT conditions are, $\forall k,m_k$,

$$-\nabla_{P_k^\star(x_{m_k})}I^\star(x_\mathcal{K})+\nu_k^\star-\lambda_{k,m_k}^\star=0,\tag{34a}$$

$$\lambda_{k,m_k}^\star=0,\quad P_k^\star(x_{m_k})>0,\tag{34b}$$

$$\lambda_{k,m_k}^\star\geq0,\quad P_k^\star(x_{m_k})=0.\tag{34c}$$

The directional derivative can be explicitly expressed as

$$\nabla_{P_k^\star(x_{m_k})}I^\star(x_\mathcal{K})=I_k^\star(x_{m_k})-(1-\rho).\tag{35}$$

Combining (34) and (35), we have

$$I_k^\star(x_{m_k})=\nu_k^\star+(1-\rho),\quad P_k^\star(x_{m_k})>0,\tag{36a}$$
$$I_k^\star(x_{m_k})\leq\nu_k^\star+(1-\rho),\quad P_k^\star(x_{m_k})=0,\tag{36b}$$

which suggests

$$\sum_{m_k}P_k^\star(x_{m_k})I_k^\star(x_{m_k})=\nu_k^\star+(1-\rho).\tag{37}$$

On the other hand, by definition of weighted sum marginal information (18),

$$\sum_{m_k}P_k^\star(x_{m_k})I_k^\star(x_{m_k})=I^\star(x_\mathcal{K}),\tag{38}$$

where the right-hand side is irrelevant to k. (36), (37), and (38) together complete the proof.

B. Proof of Proposition 2

We first prove sequence (23) is non-decreasing in weighted sum mutual information. Let $P_\mathcal{K}(x_{m_\mathcal{K}})=\prod_{q\in\mathcal{K}}P_q(x_{m_q})$ and $P_\mathcal{K}'(x_{m_\mathcal{K}})=P_k'(x_{m_k})\prod_{q\in\mathcal{K}\setminus\{k\}}P_q(x_{m_q})$ be two probability distributions with potentially different marginal for tag $k\in\mathcal{K}$ at state $m_k\in\mathcal{M}$, and define an intermediate function $J(P_\mathcal{K}(x_{m_\mathcal{K}}),P_\mathcal{K}'(x_{m_\mathcal{K}}))$ as (39) at the end of page 11. It is straightforward to verify $J(P_\mathcal{K}(x_{m_\mathcal{K}}),P_\mathcal{K}(x_{m_\mathcal{K}}))=I(x_\mathcal{K})$ and $J(P_\mathcal{K}(x_{m_\mathcal{K}}),P_\mathcal{K}'(x_{m_\mathcal{K}}))$ is a concave function for a fixed $P_\mathcal{K}'(x_{m_\mathcal{K}})$. By choosing $\nabla_{P_k^\star(x_{m_k})}J(P_\mathcal{K}(x_{m_\mathcal{K}}),P_\mathcal{K}'(x_{m_\mathcal{K}}))=0$, we have

$$S_k'(x_{m_k})-S_k'(x_{i_k})+(1-\rho)\log\frac{P_k(x_{i_k})}{P_k^\star(x_{m_k})}=0,\tag{40}$$

where $i_k\neq m_k$ is the reference state and

$$S_k'(x_{m_k})\triangleq I_k'(x_{m_k})+(1-\rho)\sum_{m_{\mathcal{K}\setminus\{k\}}}P_{\mathcal{K}\setminus\{k\}}(x_{m_{\mathcal{K}\setminus\{k\}}})$$
$$\times\sum_{m_\mathcal{K}'}P(\hat{x}_{m_\mathcal{K}'}|x_{m_\mathcal{K}})\log P_\mathcal{K}'(x_{m_\mathcal{K}}).\tag{41}$$

Evidently, $\forall m_k\neq i_k$, (40) boils down to

$$P_k^\star(x_{m_k})=\frac{P_k'(x_{m_k})\exp\left(\frac{\rho}{1-\rho}I_k'(x_{m_k})\right)}{\sum_{m_k'}P_k'(x_{m_k'})\exp\left(\frac{\rho}{1-\rho}I_k'(x_{m_k'})\right)}.\tag{42}$$

We also notice $P_k(x_{i_k}) = 1 - \sum_{m_k \neq i_k} P_k^\star(x_{m_k})$ has exactly the same expression as (42). Therefore, the result is irrelevant to the choice of reference state, and (42) is indeed optimal $\forall m_k \in \mathcal{M}$. That is, for a fixed $P_{\mathcal{K}}'(x_{m_{\mathcal{K}}})$, choosing $P_k(x_{m_k})$ by (42) ensures

$$J(P_{\mathcal{K}}(x_{m_{\mathcal{K}}}), P_{\mathcal{K}}'(x_{m_{\mathcal{K}}})) \geq I'(x_{\mathcal{K}}). \tag{43}$$

On the other hand, it also guarantees

$$\Delta \triangleq I(x_{\mathcal{K}}) - J(P_{\mathcal{K}}(x_{m_{\mathcal{K}}}), P_{\mathcal{K}}'(x_{m_{\mathcal{K}}})) \tag{44a}$$

$$= (1-\rho) \sum_{m_k} \frac{P_k'(x_{m_k}) f_k'(x_{m_k})}{\sum_{m_k'} P_k'(x_{m_k'}) f_k'(x_{m_k'})} \sum_{m_{\mathcal{K}}''} P(\hat{x}_{m_{\mathcal{K}}''} | x_{m_k})$$

$$\times \log \frac{\sum_{m_k'} P_k'(x_{m_k'}) P(\hat{x}_{m_{\mathcal{K}}''} | x_{m_{k'}}) f_k'(x_{m_k})}{\sum_{m_k'} P_k'(x_{m_k'}) P(\hat{x}_{m_{\mathcal{K}}''} | x_{m_{k'}}) f_k'(x_{m_{k'}})} \tag{44b}$$

$$\geq (1-\rho) \sum_{m_k} \frac{P_k'(x_{m_k}) f_k'(x_{m_k})}{\sum_{m_k'} P_k'(x_{m_k'}) f_k'(x_{m_k'})} \sum_{m_{\mathcal{K}}''} P(\hat{x}_{m_{\mathcal{K}}''} | x_{m_k})$$

$$\times \left(1 - \frac{\sum_{m_k'} P_k'(x_{m_k'}) P(\hat{x}_{m_{\mathcal{K}}''} | x_{m_{k'}}) f_k'(x_{m_{k'}})}{\sum_{m_k'} P_k'(x_{m_k'}) P(\hat{x}_{m_{\mathcal{K}}''} | x_{m_{k'}}) f_k'(x_{m_k})} \right) \tag{44c}$$

$$= 0, \tag{44d}$$

where $f_k'(x_{m_k}) \triangleq \exp\left(\frac{\rho}{1-\rho} I_k'(x_{m_k}) \right)$ and the equality holds if and only if (42) converges. (43) and (44) together imply $I(x_{\mathcal{K}}) \geq I'(x_{\mathcal{K}})$. Since mutual information is bounded above, we conclude the sequence (23) is non-decreasing and convergent in mutual information.

Next, we prove any converging point of sequence (23), denoted as $P_k^\star(x_{m_k})$, fulfills KKT conditions (22). To see this, define

$$D_k^{(r)}(x_{m_k}) \triangleq \frac{P_k^{(r+1)}(x_{m_k})}{P_k^{(r)}(x_{m_k})} = \frac{f_k^{(r)}(x_{m_k})}{\sum_{m_k'} P_k^{(r)}(x_{m_k'}) f_k^{(r)}(x_{m_k'})}. \tag{45}$$

As sequence (23) is convergent, any state with $P_k^\star(x_{m_k}) > 0$ need to satisfy $D_k^\star(x_{m_k}) \triangleq \lim_{r \to \infty} D_k^{(r)}(x_{m_k}) = 1$, namely

$$I_k^\star(x_{m_k}) = \frac{1-\rho}{\rho} \log \sum_{m_k'} P_k^\star(x_{m_k'}) f_k^\star(x_{m_k'}), \tag{46}$$

which is reminiscent of (36a) and (22a). That is to say, given $P_k^{(0)}(x_{m_k}) > 0$, any converging point with $P_k^\star(x_{m_k}) > 0$ must satisfy (22a). On the other hand, we assume $P_k^\star(x_{m_k})$ does not satisfy (22b), such that for any state with $P_k^\star(x_{m_k}) = 0$,

$$I_k^\star(x_{m_k}) > I^\star(x_{\mathcal{K}}) = \sum_{m_k'} P_k^\star(x_{m_k'}) I_k^\star(x_{m_k'}), \tag{47}$$

where the equality inherits from (19). Since exponential function is monotonically increasing, we have $f_k^\star(x_{m_k}) >$

$\sum_{m_k'} P_k^\star(x_{m_k'}) f_k^\star(x_{m_k'})$ and $D_k^\star(x_{m_k}) > 1$. Considering $P_k^{(0)}(x_{m_k}) > 0$ and $P_k^\star(x_{m_k}) = 0$, it contradicts with

$$P_k^{(r)}(x_{m_k}) = P_k^{(0)}(x_{m_k}) \prod_{n=1}^{r} D_k^{(n)}(x_{m_k}). \tag{48}$$

Therefore, given $P_k^{(0)}(x_{m_k}) > 0$, any converging point with $P_k^\star(x_{m_k}) = 0$ must satisfy (22b). This completes the proof.

REFERENCES

[1] C. Boyer and S. Roy, "Backscatter communication and rfid: Coding, energy, and mimo analysis," *IEEE Transactions on Communications*, vol. 62, pp. 770–785, 3 2014. [Online]. Available: http://ieeexplore.ieee.org/document/6685977/

[2] D. Dobkin, *The RF in RFID: Passive UHF RFID in Practice*. Newnes, 11 2012. [Online]. Available: https://www.elsevier.com/books/the-rf-in-rfid/dobkin/978-0-12-394583-9

[3] J. Landt, "The history of rfid," *IEEE Potentials*, vol. 24, pp. 8–11, 10 2005.

[4] G. Vannucci, A. Bletsas, and D. Leigh, "A software-defined radio system for backscatter sensor networks," *IEEE Transactions on Wireless Communications*, vol. 7, pp. 2170–2179, 6 2008. [Online]. Available: http://ieeexplore.ieee.org/document/4543069/

[5] S. D. Assimonis, S. N. Daskalakis, and A. Bletsas, "Sensitive and efficient rf harvesting supply for batteryless backscatter sensor networks," *IEEE Transactions on Microwave Theory and Techniques*, vol. 64, pp. 1327–1338, 4 2016.

[6] V. Liu, A. Parks, V. Talla, S. Gollakota, D. Wetherall, and J. R. Smith, "Ambient backscatter: Wireless communication out of thin air," *ACM SIGCOMM Computer Communication Review*, vol. 43, pp. 39–50, 9 2013. [Online]. Available: https://dl.acm.org/doi/10.1145/2534169.2486015

[7] G. Yang, Q. Zhang, and Y.-C. Liang, "Cooperative ambient backscatter communications for green internet-of-things," *IEEE Internet of Things Journal*, vol. 5, pp. 1116–1130, 4 2018. [Online]. Available: https://ieeexplore.ieee.org/document/8274950/

[8] Y.-C. Liang, Q. Zhang, E. G. Larsson, and G. Y. Li, "Symbiotic radio: Cognitive backscattering communications for future wireless networks," *IEEE Transactions on Cognitive Communications and Networking*, vol. 6, pp. 1242–1255, 12 2020. [Online]. Available: https://ieeexplore.ieee.org/document/9193946/

[9] H. Guo, Y.-C. Liang, R. Long, and Q. Zhang, "Cooperative ambient backscatter system: A symbiotic radio paradigm for passive iot," *IEEE Wireless Communications Letters*, vol. 8, pp. 1191–1194, 8 2019. [Online]. Available: https://ieeexplore.ieee.org/document/8692391/

[10] H. Ding, D. B. da Costa, and J. Ge, "Outage analysis for cooperative ambient backscatter systems," *IEEE Wireless Communications Letters*, vol. 9, pp. 601–605, 5 2020. [Online]. Available: https://ieeexplore.ieee.org/document/8941106/

[11] Q. Zhang, Y.-C. Liang, H.-C. Yang, and H. V. Poor, "Mutualistic mechanism in symbiotic radios: When can the primary and secondary transmissions be mutually beneficial?" *IEEE Transactions on Wireless Communications*, vol. 1276, pp. 1–1, 2022. [Online]. Available: https://ieeexplore.ieee.org/document/9751388/

[12] R. Long, Y.-C. Liang, H. Guo, G. Yang, and R. Zhang, "Symbiotic radio: A new communication paradigm for passive internet of things," *IEEE Internet of Things Journal*, vol. 7, pp. 1350–1363, 2 2020. [Online]. Available: https://ieeexplore.ieee.org/document/8907447/

[13] S. Zhou, W. Xu, K. Wang, C. Pan, M.-S. Alouini, and A. Nallanathan, "Ergodic rate analysis of cooperative ambient backscatter communication," *IEEE Wireless Communications Letters*, vol. 8, pp. 1679–1682, 12 2019. [Online]. Available: https://ieeexplore.ieee.org/document/8807353/

$$J(P_{\mathcal{K}}(x_{m_{\mathcal{K}}}), P_{\mathcal{K}}'(x_{m_{\mathcal{K}}})) \triangleq \rho \sum_{m_{\mathcal{K}}} P_{\mathcal{K}}(x_{m_{\mathcal{K}}}) \log \left(1 + \frac{|\boldsymbol{h}_{\mathrm{E}}^H(x_{m_{\mathcal{K}}}) \boldsymbol{w}|^2}{\sigma_v^2} \right)$$

$$+ (1-\rho) \sum_{m_{\mathcal{K}}} P_{\mathcal{K}}(x_{m_{\mathcal{K}}}) \sum_{m_{\mathcal{K}}'} P(\hat{x}_{m_{\mathcal{K}}'} | x_{m_{\mathcal{K}}}) \log \frac{P(\hat{x}_{m_{\mathcal{K}}'} | x_{m_{\mathcal{K}}}) P_{\mathcal{K}}'(x_{m_{\mathcal{K}}})}{P'(\hat{x}_{m_{\mathcal{K}}'}) P_{\mathcal{K}}(x_{m_{\mathcal{K}}})}. \tag{39}$$

[14] T. Wu, M. Jiang, Q. Zhang, Q. Li, and J. Qin, "Beamforming design in multiple-input-multiple-output symbiotic radio backscatter systems," *IEEE Communications Letters*, vol. 25, pp. 1949–1953, 6 2021. [Online]. Available: https://ieeexplore.ieee.org/document/9358202/

[15] J. Xu, Z. Dai, and Y. Zeng, "Enabling full mutualism for symbiotic radio with massive backscatter devices," *arXiv:2106.05789*, 6 2021. [Online]. Available: http://arxiv.org/abs/2106.05789

[16] H. Yang, Y. Ye, K. Liang, and X. Chu, "Energy efficiency maximization for symbiotic radio networks with multiple backscatter devices," *IEEE Open Journal of the Communications Society*, vol. 2, pp. 1431–1444, 2021. [Online]. Available: https://ieeexplore.ieee.org/document/9461158/

[17] S. Han, Y.-C. Liang, and G. Sun, "The design and optimization of random code assisted multi-bd symbiotic radio system," *IEEE Transactions on Wireless Communications*, vol. 20, pp. 5159–5170, 8 2021. [Online]. Available: https://ieeexplore.ieee.org/document/9382925/

[18] G. Vougioukas and A. Bletsas, "Switching frequency techniques for universal ambient backscatter networking," *IEEE Journal on Selected Areas in Communications*, vol. 37, pp. 464–477, 2 2019. [Online]. Available: https://ieeexplore.ieee.org/document/8474355/

[19] Q. Wu, S. Zhang, B. Zheng, C. You, and R. Zhang, "Intelligent reflecting surface-aided wireless communications: A tutorial," *IEEE Transactions on Communications*, vol. 69, pp. 3313–3351, 5 2021. [Online]. Available: https://ieeexplore.ieee.org/document/9326394/

[20] Q. Wu and R. Zhang, "Intelligent reflecting surface enhanced wireless network: Joint active and passive beamforming design," vol. 18. IEEE, 12 2018, pp. 1–6. [Online]. Available: https://ieeexplore.ieee.org/document/8647620/

[21] S. Zhang and R. Zhang, "Capacity characterization for intelligent reflecting surface aided mimo communication," *IEEE Journal on Selected Areas in Communications*, vol. 38, pp. 1823–1838, 8 2020. [Online]. Available: https://ieeexplore.ieee.org/document/9110912/

[22] S. Lin, B. Zheng, F. Chen, and R. Zhang, "Intelligent reflecting surface-aided spectrum sensing for cognitive radio," *IEEE Wireless Communications Letters*, vol. 11, pp. 928–932, 5 2022.

[23] Y. Liu, Y. Zhang, X. Zhao, S. Geng, P. Qin, and Z. Zhou, "Dynamic-controlled ris assisted multi-user miso downlink system: Joint beamforming design," *IEEE Transactions on Green Communications and Networking*, vol. 6, pp. 1069–1081, 6 2022.

[24] Z. Feng, B. Clerckx, and Y. Zhao, "Waveform and beamforming design for intelligent reflecting surface aided wireless power transfer: Single-user and multi-user solutions," *IEEE Transactions on Wireless Communications*, 2022.

[25] Y. Zhao, B. Clerckx, and Z. Feng, "Irs-aided swipt: Joint waveform, active and passive beamforming design under nonlinear harvester model," *IEEE Transactions on Communications*, vol. 70, pp. 1345–1359, 2022.

[26] Q. Wu, X. Zhou, and R. Schober, "Irs-assisted wireless powered noma: Do we really need different phase shifts in dl and ul?" *arXiv:2102.08739*, vol. 10, pp. 1493–1497, 7 2021. [Online]. Available: https://ieeexplore.ieee.org/document/9400380/

[27] Q. Wu, X. Zhou, W. Chen, J. Li, and X. Zhang, "Irs-aided wpcns: A new optimization framework for dynamic irs beamforming," *IEEE Transactions on Wireless Communications*, pp. 1–1, 12 2021.

[28] M. Hua and Q. Wu, "Joint dynamic passive beamforming and resource allocation for irs-aided full-duplex wpcn," *IEEE Transactions on Wireless Communications*, pp. 1–1, 12 2021.

[29] R. Karasik, O. Simeone, M. D. Renzo, and S. S. Shitz, "Beyond max-snr: Joint encoding for reconfigurable intelligent surfaces," vol. 2020-June. IEEE, 6 2020, pp. 2965–2970. [Online]. Available: https://ieeexplore.ieee.org/document/9174060/

[30] R. Liu, H. Li, M. Li, and Q. Liu, "Symbol-level precoding design for intelligent reflecting surface assisted multi-user mimo systems." IEEE, 10 2019, pp. 1–6. [Online]. Available: https://ieeexplore.ieee.org/document/8928065/

[31] A. Bereyhi, V. Jamali, R. R. Muller, A. M. Tulino, G. Fischer, and R. Schober, "A single-rf architecture for multiuser massive mimo via reflecting surfaces." IEEE, 5 2020, pp. 8688–8692. [Online]. Available: https://ieeexplore.ieee.org/document/9052989/

[32] X. Xu, Y.-C. Liang, G. Yang, and L. Zhao, "Reconfigurable intelligent surface empowered symbiotic radio over broadcasting signals," vol. 2020-Janua. IEEE, 12 2020, pp. 1–6. [Online]. Available: https://ieeexplore.ieee.org/document/9348236/

[33] Q. Zhang, Y.-C. Liang, and H. V. Poor, "Reconfigurable intelligent surface assisted mimo symbiotic radio networks," *IEEE Transactions on Communications*, vol. 69, pp. 4832–4846, 7 2021. [Online]. Available: https://ieeexplore.ieee.org/document/9391685/

[34] J. Hu, Y. C. Liang, and Y. Pei, "Reconfigurable intelligent surface enhanced multi-user miso symbiotic radio system," *IEEE Transactions on Communications*, vol. 69, pp. 2359–2371, 4 2021.

[35] M. Hua, Q. Wu, L. Yang, R. Schober, and H. V. Poor, "A novel wireless communication paradigm for intelligent reflecting surface based symbiotic radio systems," *IEEE Transactions on Signal Processing*, vol. 70, pp. 550–565, 4 2022. [Online]. Available: http://arxiv.org/abs/2104.09161https://ieeexplore.ieee.org/document/9652042/

[36] E. Basar, "Reconfigurable intelligent surface-based index modulation: A new beyond mimo paradigm for 6g," *IEEE Transactions on Communications*, vol. 68, pp. 3187–3196, 5 2020. [Online]. Available: https://ieeexplore.ieee.org/document/8981888/

[37] T. Ma, Y. Xiao, X. Lei, P. Yang, X. Lei, and O. A. Dobre, "Large intelligent surface assisted wireless communications with spatial modulation and antenna selection," *IEEE Journal on Selected Areas in Communications*, vol. 38, pp. 2562–2574, 11 2020. [Online]. Available: https://ieeexplore.ieee.org/document/9133588/

[38] J. Yuan, M. Wen, Q. Li, E. Basar, G. C. Alexandropoulos, and G. Chen, "Receive quadrature reflecting modulation for ris-empowered wireless communications," *IEEE Transactions on Vehicular Technology*, vol. 70, pp. 5121–5125, 5 2021. [Online]. Available: https://ieeexplore.ieee.org/document/9405433/

[39] S. Hu, C. Liu, Z. Wei, Y. Cai, D. W. K. Ng, and J. Yuan, "Beamforming design for intelligent reflecting surface-enhanced symbiotic radio systems," *arxiv:2110.10316*, 10 2021. [Online]. Available: http://arxiv.org/abs/2110.10316

[40] Y. Huang, A. Alieldin, and C. Song, "Equivalent circuits and analysis of a generalized antenna system," *IEEE Antennas and Propagation Magazine*, vol. 63, pp. 53–62, 4 2021. [Online]. Available: https://ieeexplore.ieee.org/document/9392844/

[41] Y. C. Liang, Q. Zhang, J. Wang, R. Long, H. Zhou, and G. Yang, "Backscatter communication assisted by reconfigurable intelligent surfaces," *Proceedings of the IEEE*, 2022.

[42] S. J. Thomas, E. Wheeler, J. Teizer, and M. S. Reynolds, "Quadrature amplitude modulated backscatter in passive and semipassive uhf rfid systems," *IEEE Transactions on Microwave Theory and Techniques*, vol. 60, pp. 1175–1182, 4 2012. [Online]. Available: http://ieeexplore.ieee.org/document/6153042/

[43] R. Hansen, "Relationships between antennas as scatterers and as radiators," *Proceedings of the IEEE*, vol. 77, pp. 659–662, 5 1989. [Online]. Available: http://ieeexplore.ieee.org/document/32056/

[44] Q. Wu and R. Zhang, "Towards smart and reconfigurable environment: Intelligent reflecting surface aided wireless network," *IEEE Communications Magazine*, vol. 58, pp. 106–112, 1 2020. [Online]. Available: https://ieeexplore.ieee.org/document/8910627/

[45] J. Zhou, P. Zhang, J. Han, L. Li, and Y. Huang, "Metamaterials and metasurfaces for wireless power transfer and energy harvesting," *Proceedings of the IEEE*, vol. 110, pp. 31–55, 1 2022.

[46] Y. Huang, *Antennas: From Theory to Practice*. Wiley, 9 2021.

[47] A. Singh, M. Andrello, N. Thawdar, and J. M. Jornet, "Design and operation of a graphene-based plasmonic nano-antenna array for communication in the terahertz band," *IEEE Journal on Selected Areas in Communications*, vol. 38, pp. 2104–2117, 9 2020.

[48] F. Costa and M. Borgese, "Electromagnetic model of reflective intelligent surfaces," *IEEE Open Journal of the Communications Society*, vol. 2, pp. 1577–1589, 2021.

[49] M. E. Bialkowski and K. H. Sayidmarie, "Investigations into phase characteristics of a single-layer reflectarray employing patch or ring elements of variable size," *IEEE Transactions on Antennas and Propagation*, vol. 56, pp. 3366–3372, 2008.

[50] D. Bharadia, K. R. Joshi, M. Kotaru, and S. Katti, "Backfi: High throughput wifi backscatter," vol. 45. ACM, 8 2015, pp. 283–296. [Online]. Available: https://dl.acm.org/doi/10.1145/2785956.2787490

[51] G. Yang, C. K. Ho, and Y. L. Guan, "Multi-antenna wireless energy transfer for backscatter communication systems," *IEEE Journal on Selected Areas in Communications*, vol. 33, pp. 2974–2987, 12 2015. [Online]. Available: http://ieeexplore.ieee.org/document/7274644/

[52] H. Guo, Q. Zhang, S. Xiao, and Y.-C. Liang, "Exploiting multiple antennas for cognitive ambient backscatter communication," *IEEE Internet of Things Journal*, vol. 6, pp. 765–775, 2 2019. [Online]. Available: https://ieeexplore.ieee.org/document/8411483/

[53] Q. Wu and R. Zhang, "Intelligent reflecting surface enhanced wireless network via joint active and passive beamforming," *IEEE Transactions on Wireless Communications*, vol. 18, pp. 5394–5409, 11 2019. [Online]. Available: https://ieeexplore.ieee.org/document/8811733/

[54] J. Qian, Y. Zhu, C. He, F. Gao, and S. Jin, "Achievable rate and capacity analysis for ambient backscatter communications," *IEEE*

Transactions on Communications, vol. 67, pp. 6299–6310, 9 2019. [Online]. Available: https://ieeexplore.ieee.org/document/8721108/

[55] T. Nguyen and T. Nguyen, "Capacity achieving quantizer design for binary channels," *IEEE Communications Letters*, vol. 25, pp. 759–763, 3 2021. [Online]. Available: https://ieeexplore.ieee.org/document/9247251/

[56] M. Rezaeian and A. Grant, "Computation of total capacity for discrete memoryless multiple-access channels," *IEEE Transactions on Information Theory*, vol. 50, pp. 2779–2784, 11 2004. [Online]. Available: http://ieeexplore.ieee.org/document/1347364/

[57] J. Buhler and G. Wunder, "A note on capacity computation for the discrete multiple access channel," *IEEE Transactions on Information Theory*, vol. 57, pp. 1906–1910, 4 2011. [Online]. Available: https://ieeexplore.ieee.org/document/5730559/

[58] G. J. O. Jameson, "The incomplete gamma functions," *The Mathematical Gazette*, vol. 100, pp. 298–306, 7 2016. [Online]. Available: https://www.cambridge.org/core/product/identifier/S002555721600067X/type/journal_article

[59] X. He, K. Cai, W. Song, and Z. Mei, "Dynamic programming for sequential deterministic quantization of discrete memoryless channels," *IEEE Transactions on Communications*, vol. 69, pp. 3638–3651, 6 2021. [Online]. Available: https://ieeexplore.ieee.org/document/9366549/

[60] T. Nguyen and T. Nguyen, "On thresholding quantizer design for mutual information maximization: Optimal structures and algorithms," vol. 2020-May. IEEE, 5 2020, pp. 1–5. [Online]. Available: https://ieeexplore.ieee.org/document/9128966/

[61] J. Qian, A. N. Parks, J. R. Smith, F. Gao, and S. Jin, "Iot communications with m-psk modulated ambient backscatter: Algorithm, analysis, and implementation," *IEEE Internet of Things Journal*, vol. 6, pp. 844–855, 2 2019. [Online]. Available: https://ieeexplore.ieee.org/document/8423609/

[62] S. Arimoto, "An algorithm for computing the capacity of arbitrary discrete memoryless channels," *IEEE Transactions on Information Theory*, vol. 18, pp. 14–20, 1 1972. [Online]. Available: http://ieeexplore.ieee.org/document/1054753/

[63] R. E. Blahut, "Computation of channel capacity and rate-distortion functions," *IEEE Transactions on Information Theory*, vol. 18, pp. 460–473, 7 1972. [Online]. Available: http://ieeexplore.ieee.org/document/1054855/

[64] E. Calvo, D. P. Palomar, J. R. Fonollosa, and J. Vidal, "On the computation of the capacity region of the discrete mac," *IEEE Transactions on Communications*, vol. 58, pp. 3512–3525, 12 2010. [Online]. Available: http://ieeexplore.ieee.org/document/5590317/

[65] C. Qiu, Q. Wu, M. Hua, X. guan, and Y. Wu, "Achieving multi-beam gain in intelligent reflecting surface assisted wireless energy transfer," *arXiv:2205.08893*, 5 2022. [Online]. Available: http://arxiv.org/abs/2205.08893